JOURNAL OF MATERIALS SCIENCE 28 (1993) 4855–4861

A study of damage under tensile loading in a new Al–Si–Fe alloy processed by the Osprey route

A. MOCELLIN, R. FOUGERES, P. F. GOBIN
GEMPPM, URA CNRS 341, INSA Lyon, bat. 303, F-69621 Villeurbanne Cedex, France

The mode of damage in tension of a new Al–Si–Fe alloy made by spray deposition was studied. This alloy has a composite type structure composed of silicon and intermetallic particles in an aluminium matrix. *In situ* tensile tests in the SEM, with gold microgrids deposited on the surface of the specimen as an indicator of local plastic strains, provide us with a better understanding of the damage process from crack initiation to fracture. In the T4 temper, the first cracks appear in silicon particles; they initiate shearings and/or decohesions in the matrix, which develop along grain boundaries. Just before the brittle failure of the sample, the generalized microcracking involves both silicon-particle cracking and grain-boundary decohesions.

1. Introduction

A new kind of aluminium-based alloy (Al–Si–Fe) has been made by the Osprey™ route. This production process presents many advantages: easy introduction of large amounts of alloying elements, fine and homogeneous microstructure, no macrosegregations and good mechanical properties at relatively low costs [1–3].

These alloys are quite different from conventional precipitation-hardened aluminium alloys, in that their structure is rather similar to that of particulate-reinforced metal matrix composites. They contain almost 30% volume fraction of particles which, in our case, are silicon and intermetallic phases. This multi-reinforcing phase allows the elastic modulus of the alloy to be considerably increased up to 90 GPa.

Other alloys with comparable microstructures have been manufactured, often from rapidly solidified powders, and studied in terms of their microstructures and mechanical properties [4–8]. More precisely, the influence of iron in Al–Si–Cu–Mg alloys has been investigated [9, 10]. Such alloys could be used in the production of pistons and connecting rods for automotive engines [11]. In fact, it seems possible to obtain good high-temperature properties [12] as well as an improved fatigue resistance in comparison with conventional aluminium alloys.

The studied alloy presents a particularly good endurance ratio (defined as the ratio of the fatigue limit to the tensile fracture stress) of 0.42, whereas the usual values for aluminium alloys are between 0.25 and 0.3 [13]. Research concerning the relation between the microstructure and the mechanical properties of this alloy under both monotonic and tensile loadings has been undertaken in our laboratory.

The aim of the present work was to obtain a better understanding of the process of damage during monotonic tensile loadings of this dispersion-strengthened aluminium alloy processed by the Osprey™ route. Consequently, *in situ* tensile tests in a scanning electron microscope (SEM), using gold grids as a micro-extensometry technique at the surface of tensile specimens, were performed.

2. Experimental procedure

2.1 Microstructure of the Al–Si–Fe alloy

The studied alloy contains approximately 14 wt % Si and 3 wt % Fe, with a small amount of other elements such as copper, magnesium, manganese and zirconium.

The aluminium matrix was strengthened with dispersed phases, silicon and intermetallics (Fig. 1). The microstructure is rather complex and not detailed in this paper. Only some essential information is given hereafter. The matrix is composed of small grains, 1–3 μm in size, with a fine and dense precipitation (Fig. 2). These precipitates could be S′-Al_2CuMg or λ′-$Al_5Cu_2Mg_8Si_6$, i.e. the type of precipitation found in the 2xxx series of alloys [14, 15], and their mean size does not exceed 10 nm. The precipitate free zone at the grain boundaries, when present was of the order of 50 nm.

The reinforcing phases were analysed with the Tracor X-ray microprobe in the SEM and can be classified into three main types:

(i) silicon particles with a size of 3–5 μm;

(ii) intermetallic compounds (AlFeSi), rod-like in shape, with a length of 1–5 μm and an aspect ratio of 3–5;

(iii) spheroidal intermetallics (AlFeMnSiCu) either small, 0.1–0.5 μm (Fig. 3) or larger, 1–3 μm.

The thermomechanical history of the alloy was as follows: the billets resulting from the spray deposition

0022–2461

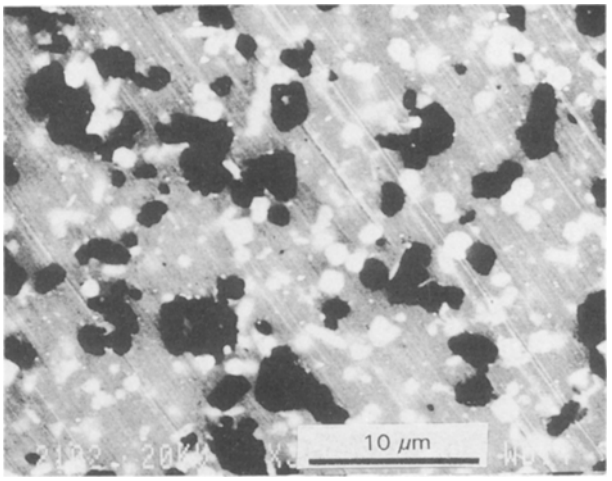

Figure 1 Scanning electron micrograph of a diamond-polished surface of the alloy; black, silicon particles; white, intermetallic particles.

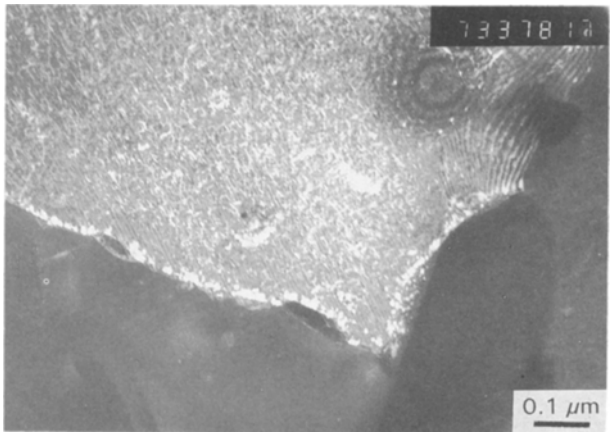

Figure 2 Transmission electron micrograph of the precipitation in the matrix (under peak-ageing conditions).

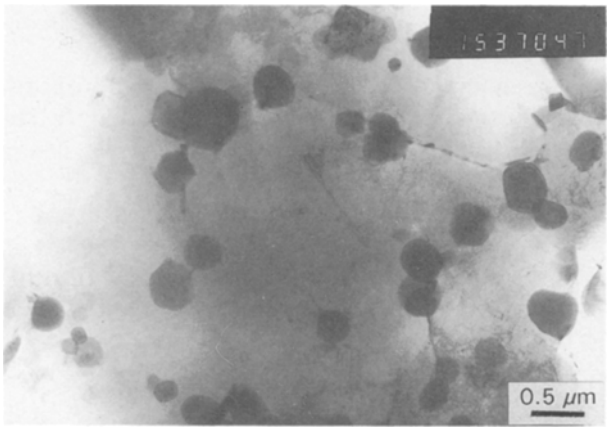

Figure 3 Transmission electron micrograph of the small rounded intermetallics; they are mainly situated at the grain boundaries.

were extruded into bars which were solution heat treated at 510 °C and water-quenched. After room temperature maturation of several days, the alloy was in the T4 temper. When aged at 180 °C (for 6 h), the alloy was in the peak-aged condition (T6 temper).

2.2. Classical mechanical characteristics

The main mechanical properties of the alloy have been deduced from conventional tensile tests. Strains were measured either with a MTS extensometer or with strain gauges. Results are summarized in Table I.

2.3 Microextensometry and tensile tests in the SEM

To specify the modes of deformation and damage of an alloy with such a fine microstructure, it is useful to have local information on strains. This is done using extensometric gold microgrids deposited on the polished surface of the specimen.

Square grids were first produced by a photo-resist technique using the electron beam of the SEM for irradiation. Then, evaporation of the metal produced microgrids (made of 0.17 μm wide lines and with a 2.25 μm pitch). Further details can be found elsewhere [16, 17].

The tensile-loading stage was fixed on the goniometric deck of the SEM. The two symmetrical mobile grips allowed the observation zone to be kept fixed, during loading. The geometry of the sample is shown in Fig. 4.

All SEM images were improved with a Crystal system.

3. Results

3.1. Microscopic mechanisms of initiation and the progression of damage during *in situ* tensile tests

In the T6 temper, the elongation of the alloy is so small that it is not possible to follow the progression of damage. The specimen fails in a brittle manner; observations are thus only made on the surface after failure. Plastic strain is concentrated in a narrow region, less than 100 μm wide, close to the fracture surface.

In the T4 temper, the damage appears more progressively and its chronology can be established in correlation with the load–displacement curve (Fig. 5). Configurations of damage are similar to those observed for the T6 temper after failure.

The following results concern a test with a T4 temper specimen. The load versus displacement curve recorded during the tensile test is given in Fig. 5.

TABLE I Tensile properties of the Al–Si–Fe alloy

Specimen state	Young's modulus (GPa)	0.2 % Proof stress (MPa)	Ultimate tensile stress (MPa)	Elongation (%)
T4 temper	86	280	415	4
T6 temper	86	390	460	1.5

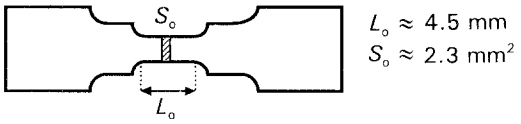

Figure 4 Geometry of the specimen for an *in situ* tensile test.

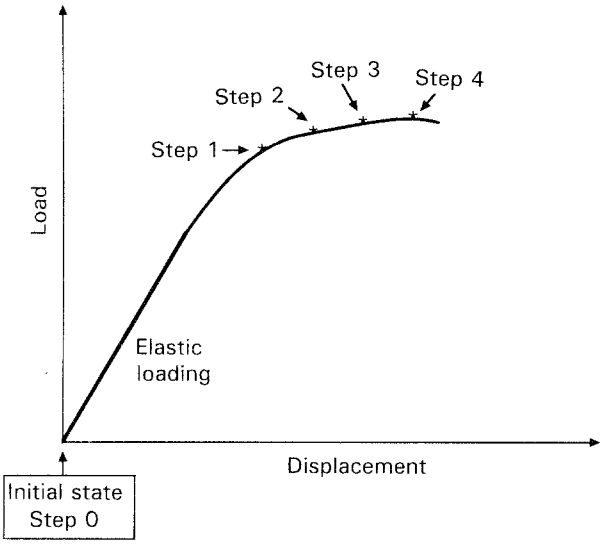

Figure 5 Load versus displacement curve recorded during the *in situ* tensile test.

Different steps in the loading are indicated with corresponding stress, (σ), and estimated macroscopic plastic strains, (ε_p), each referring to particular figures.

Step 0: initial state (Fig. 6). Silicon particles appear black and intermetallics white in the secondary electron image. However, it must be noted that after irradiation, due to the electron beam, the black colour of silicon is changed to a clear grey. The tensile axis is horizontal for all photographs.

Nothing was visualized during the elastic loading.

Step 1: $\sigma = 350$ MPa, $\varepsilon_p = 1$ % (Fig. 7). Slight deformations of the matrix are observed in the vicinity of silicon particles. In fact, bars of the microgrid in this region have lost their perfect straightness at this step (see A, Fig. 7).

Step 2: $\sigma = 380$ MPa, $\varepsilon_p = 1.8$ % (Fig. 8). Cracking of the silicon particles appears first on the larger ones,

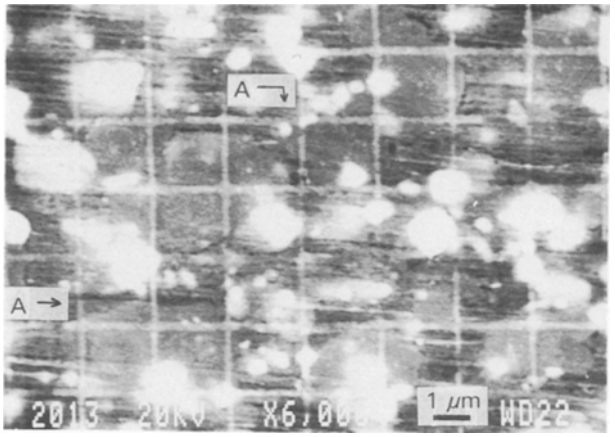

Figure 6 Initial state of the observed zone. The tensile axis is horizontal.

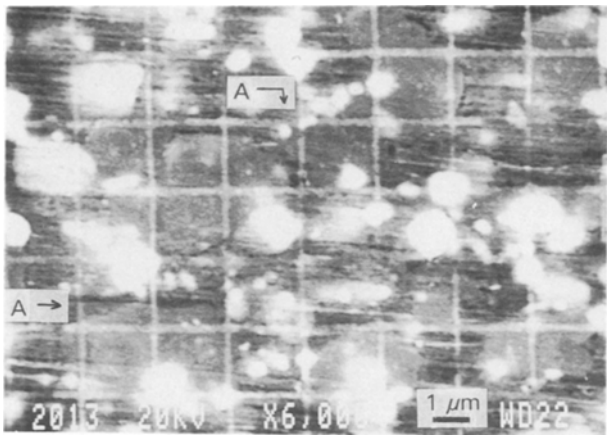

Figure 7 Beginning of the matrix deformation (same zone).

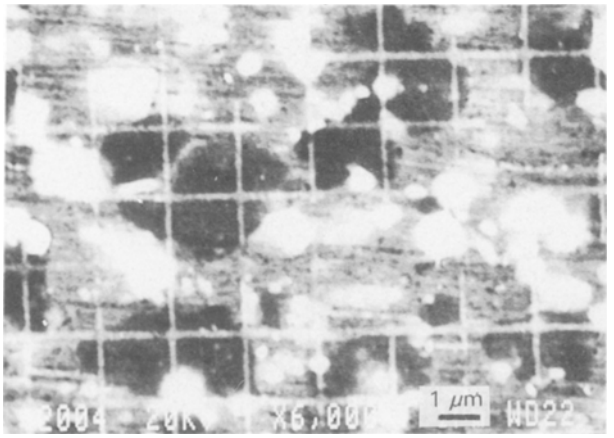

Figure 8 Cracking of silicon particles; the tensile axis is horizontal on the photograph (same zone).

and always perpendicular to the tensile axis. The matrix localized deformations become more pronounced.

Step 3: $\sigma = 395$ MPa, $\varepsilon_p = 2.5$ % (Fig. 9). Other silicon particles break while the existing cracks in the silicon open into rectangular shaped cracks. Near these cracks in the matrix, particular SEM images such as shearing bands can be observed, due to differences in plastic deformation between the grains and they develop in the matrix according to grain boundaries having an average direction of about 45° with respect to the tensile axis (Fig. 10 and see Fig. 17 later).

When a spheroidal intermetallic particle is close to the silicon particle crack, it prevents the crack growing in the matrix by favouring crack propagation at the intermetallic/matrix interface.

Step 4: $\sigma = 405$ MPa, $\varepsilon_p = 3.5$ %. Just before failure of the specimen, the microcracking is generalized (Fig. 11) including cracking of silicon particles and grain-boundary decohesions. The microgrid bars exhibit an undulated aspect indicating heterogeneous plastic strains of the different grains (Fig. 12).

Neither cracking of intermetallics nor decohesion of the silicon matrix interface occur. Favourable paths for the final crack appear (Fig. 13). The final failure takes place as the microcracks join together.

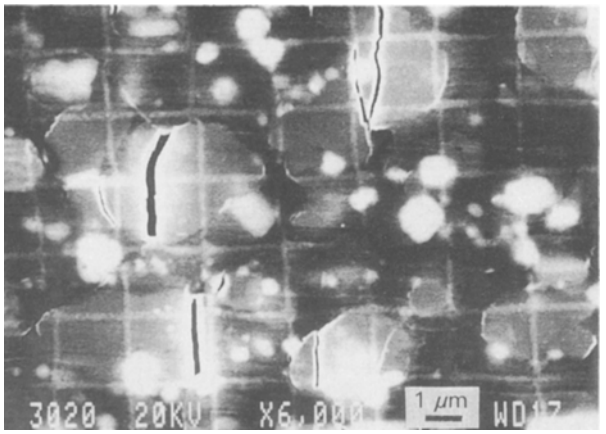

Figure 9 Progression of damage from cracked silicon particles (same zone).

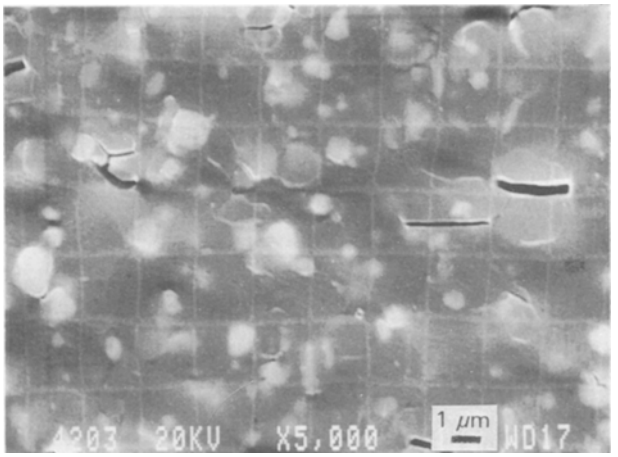

Figure 12 Undulated bars of the grid.

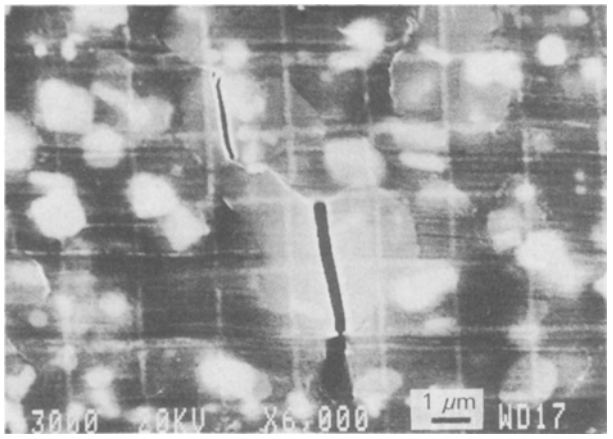

Figure 10 Shearing between two silicon particles.

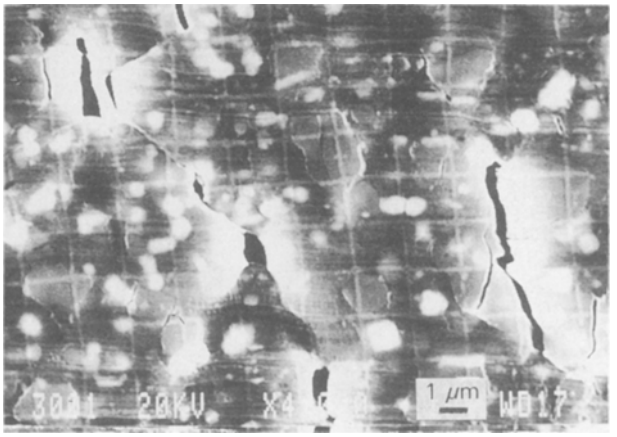

Figure 13 Views of the privileged paths for the macroscopic crack.

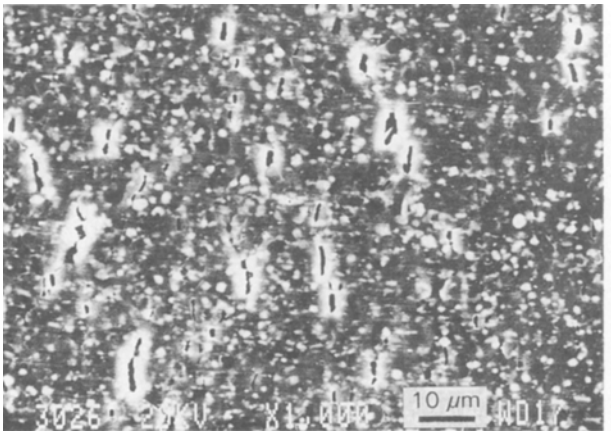

Figure 11 Microcracked aspect of the specimen.

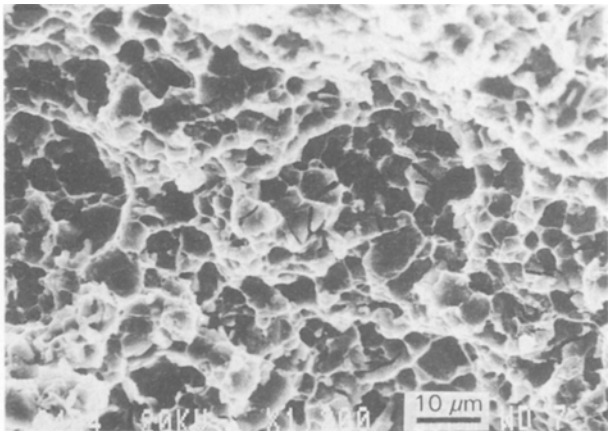

Figure 14 Aspect of the fracture surface.

3.2. Microfractography

The fracture surface is rather flat and constituted of small dimples (Fig. 14). Ridges run along grain boundaries and intermetallic matrix interfaces; this introduces a quasi-ductile aspect in the process of fracture. Cracked silicon particles are visible on the surface, as well as many small intermetallic particles in the dimples (Fig. 15).

4. Discussion

Microfractographic observations have been performed on the *in situ* tensile specimen as well as on conventional tensile specimens. It is shown that the microfractographic characteristics of fracture are identical at each point of the fracture surface. In this way our study shows that the correlation established between the damage and plastic deformation modes

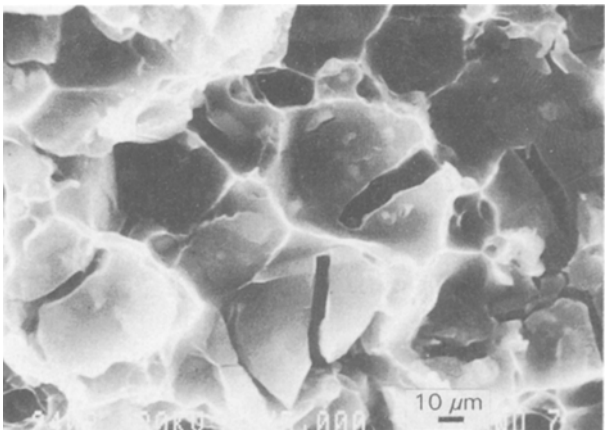

Figure 15 Detail of the fracture surface.

visualized in the vicinity of the surface are indicative of what happens in the centre of the specimen.

4.1. Fracture of silicon particles

The cracking of the silicon particles is the first cause of damage initiation in the alloy, occurring after a certain amount of plastic strain in the matrix. This plastic strain is very heterogeneous, as shown by the shearing of the grid. This heterogeneity is probably due to the presence of silicon and intermetallic particles but also to a small grain size like the dimension of the gold grid mesh line (Fig. 12).

As the applied stress is increased, silicon particles are broken because a critical tensile stress level is reached within them. The critical applied stress value for which silicon particles are broken, depends on different factors: the thermally induced internal stresses in silicon and also the stress concentration effect due to plastic deformation of the aluminium alloy matrix around the silicon particles. In fact, a variation in these factors delaying the appearance of the critical tensile stress level in the silicon particles is favourable. The stress concentration effect is generally reduced by decreasing grain size, which is effectively reached by the spray route in the case of this aluminium alloy. Thermally induced internal stresses correspond to a compressive stress field in the silicon. Any parameter which could increase this compressive internal stress field in the particles delays the beginning of damage. Calculations have been performed using an iterative Eshelby method developed in our laboratory [18]: it is shown that the shape and distribution of the intermetallic particles have an influence on the internal stress level in silicon particles. For example, Fig. 16 shows the variations of the σ_{33}^{Si} component of the internal stress field in silicon particles with the aspect ratio and distribution of intermetallic particles. The thermal loading considered is the drop of temperature at the end of the T6 heat treatment $\Delta T = -155$ K. Elastic stress fields are calculated with the hypothesis of perfectly bonded interfaces. In this case they are hydrostatic. The elastic constants and volume fractions of particles taken for these calculations are given in Table II. Young's modulus and Poisson's ratio of the iron phases have been estimated [22] from stiffness coefficients measured by an ultrasonic method [21].

Each curve of Fig. 16 corresponds to a particular distribution of intermetallic particles: upper curve, all particles are aligned with the tensile 3-axis; lower curve, the particle distribution is isotropic. In all cases, when the aspect ratio of intermetallics increases, the σ_{33}^{Si} component of the stress field in silicon particles according to the tensile 3-axis increases. This means that an alloy which contains only spherical intermetallics will be more interesting from an internal stresses point of view than an alloy with ellipsoidal intermetallics only: the fracture of silicon could be delayed in the first alloy due to a higher initial compressive stress level.

4.2. Creation of a macroscopic crack

The macroscopic crack forms by the joining of some microcracks due to silicon particle cracking (Fig. 17). The crack advance occurs along privileged paths constituted by intermetallic/matrix interfaces and grain boundaries (the precipitate-free zone may favour decohesion).

The great density of grain boundaries (small grain size) and interfaces contribute to delay the crack

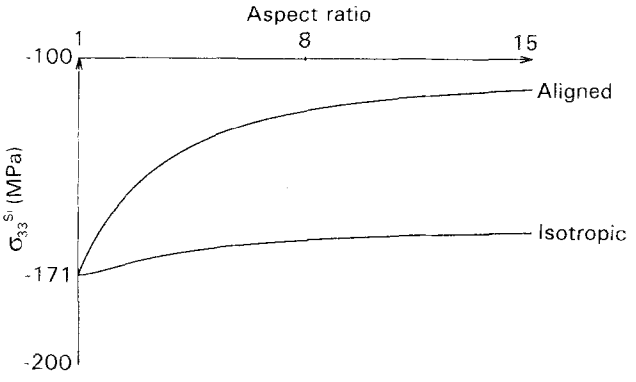

Figure 16 Internal stress field in silicon particles.

TABLE II Elastic constants used for Eshelby calculations

	Aluminium matrix	Silicon particles [19, 20]	Iron phases [21, 22]
Young's modulus, E (GPa)	70	165	250
Poisson's ratio, ν	0.33	0.22	0.21
Linear coefficient of thermal expansion, α (K^{-1})	23.5×10^{-6}	3.0×10^{-6}	3.5×10^{-6}
Volume fraction, f		0.16	0.12

advance: its path is more tortuous and longer. This remark assumes great importance when considering the high-cycle fatigue life.

4.3. Propagation of the crack

Once created, the macroscopic crack propagates instantaneously and the fracture of the specimen has a brittle aspect.

In addition to SEM observations, there exists several indirect methods to characterize and evaluate damage by creation of interfaces, which consist in measuring the evolution of physical or mechanical parameters [23]. One of them is the elastic modulus which can be easily measured and which decreases with increasing damage. An experimental and theoretical study develops this aspect in the case of an Al–Si–Mg alloy [24]. Our results show a loss of about 10% of the initial elastic modulus value after a 4% plastic strain (Fig. 18). The loss of modulus begins when the first cracking of silicon occurs at step 2 and occurs progressively over the whole plastic strain range. However, it would be interesting to perform an analysis of the unloading stiffness [25]; this gives much more accurate information on the state of damage, at least in the case of pure polycrystalline aluminium.

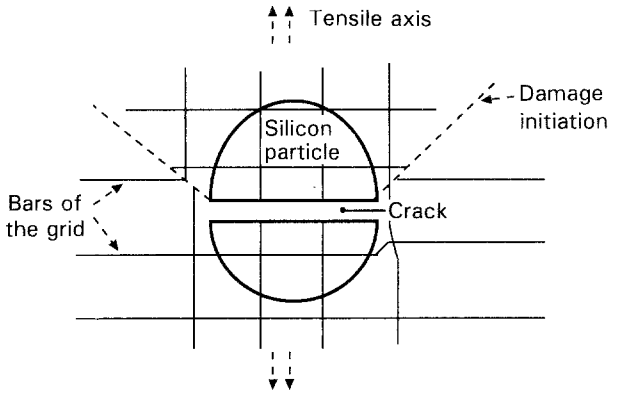

Figure 17 Schematic illustration of damage initiated at silicon particles.

5. Conclusion

The damaging process of an Al–Si–Fe alloy made by spray deposition and including different kinds of particles has been investigated. The results presented deal with tensile loading of the T4 temper alloy.

As in other silicon-dispersed aluminium alloys [8, 24, 26], cracking of primary silicon particles is one of the main features of damage. It is associated with a loss of elastic modulus.

The presence of the gold microgrids at the surface of the tensile specimen provides typical information, such as the beginning of localized plastic strain, grain-boundary shearing and strain heterogeneities between two neighbouring zones.

Acknowledgements

This work was supported by the Pechiney company CRV (Centre de Recherches de Voreppe), which is fully acknowledged. We particularly thank P. Jarry and M. Courbière for useful discussions.

References

1. J. DUSZCZYK, J. L. ESTRADA, B. M. KOREVAAR and T. L. J. DE HAAN, in "Modern Developments of Powder Metallurgy", **19** Vol., edited by P. U. Gummeson and D. A. Gustafson (Florida, 1988) p. 441.
2. J. L. ESTRADA and J. DUSZCZYK, *J. Mater. Sci.* **25** (1990) 1381.
3. J. ZHOU, J. DUSZCZYK and B. M. KOREVAAR, *ibid.* **26** (1991) 5275.
4. T. HIRANO and T. FUJITA, *J. Jpn. Inst. Light Met.* **37** (1987) 670.
5. T. FUJITA, F. KIYOTA, T. HIRANO and Y. KOJIMA, *ibid.* **37** (1987) 677.
6. S. INUMARU and A. KIKUCHI, *Sumitomo Light Met. Technol. Rep.* **29** (1988) 64.
7. H. EGASHIRA, M. NIINOMI, T. KOBAYASHI and S. KOHMURA, *J. Jpn. Inst. Light Met.* **39** (1989) 878.
8. J. ZHOU and J. DUSZCZYK, *J. Mater. Sci.* **25** (1990) 4541.
9. J. ZHOU, J. DUSZCZYK and B. M. KOREVAAR, *ibid.* **26** (1991) 824.
10. *Idem, ibid.* **26** (1991) 3041.
11. Y. TAKEDA, T. HAYASHI, Y. ODANI, N. AMANO and N. KUROISHI, in "Modern Developments of Powder Metallurgy", Vol. **19**. edited by P. U. Gummeson and D. A. Gustafson (Florida, 1988) p. 533.

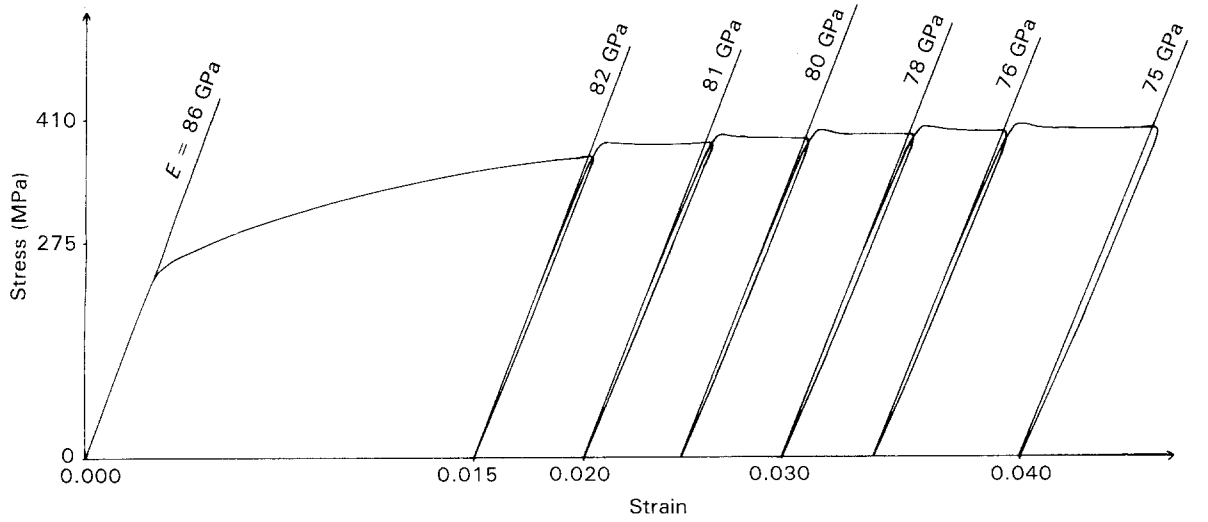

Figure 18 Measurement of elastic moduli at different plastic strains.

12. D. J. SKINNER, R. L. BYE, D. RAYBOULD and A. M. BROWN, *Scripta Metall.* **20** (1986) 867.
13. P. JARRY and M. COURBIERE, private communication (1991).
14. M. C. CHATURVEDI, A. K. GUPTA and A. K. JENA, *Mater. Sci. Eng.* **A110** (1989) 187.
15. S. ZAFAR, NAZMA IKRAM, M. A. SHAIKH and K. A. SHOAIB, *J. Mater. Sci.* **25** (1990) 2595.
16. M.-H. AMBROISE, T. BRETHEAU and A. ZAOUI, in "Micromechanics and Inhomogeneity", edited by G. J. Weng, M. Taya and H. Abé (New York, 1990) p. 41.
17. A. KARIMI, *Mater. Sci. Eng.* **63** (1984) 267.
18. R. HAMANN, A. MOCELLIN, P. F. GOBIN and R. FOUGERES, *Scripta Metall. Mater.* **26** (1992) 963.
19. G. SIMMONS and H. WANG, "Single crystal elastic constants and calculated aggregate properties: A Handbook", 2nd Edn (Cambridge, 1971) p. 370.
20. P. VAN MOURIK, Th. H. DE KEIJSER, N. M. VAN DER PERS, E. J. MITTEMEIJER, *Scripta Metall.* **22** (1988) 1547.
21. G. KÖTTER, K. NEMBACH, F. WALLOW, E. NEMBACH, *Mater. Sci. Eng.* **A114** (1989) 29.
22. J. P. HIRTH and J. LOTHE, "Theory of dislocations", 2nd Edn, (New York, 1982) p. 857.
23. B. BAUDELET and F. BARLAT, in "Physique et Mécanique de la Mise en Forme des Métaux", edited by F. Moussy and P. Franciosi (Paris, 1990) p. 180.
24. W. H. HUNT Jr, J. R. BROCKENBROUGH and P. E. MAGNUSEN, *Scripta Metall. Mater.* **25** (1991) 15.
25. A. HAMEL, A. VINCENT and R. FOUGERES, *Acta Metall.* **38** (1990) 301.
26. A. GANGULEE and J. GURLAND, *Trans. Met. Soc. AIME* **239** (1967) 269.

Received 30 March 1992
and accepted 24 February 1993